4D XCAT phantom for multimodality imaging research

W. P. Segars[a]
Department of Radiology, Carl E. Ravin Advanced Imaging Laboratories, Duke University Medical Center, 2424 Erwin Road, Hock Plaza, Suite 302, Durham, North Carolina 27705

G. Sturgeon
Department of Radiology, Carl E. Ravin Advanced Imaging Laboratories, Duke University Medical Center, 2424 Erwin Road, Hock Plaza, Suite 302, Durham, North Carolina 27705 and Department of Biomedical Engineering, The University of North Carolina, Chapel Hill, North Carolina 27599

S. Mendonca and Jason Grimes
Department of Radiology, Carl E. Ravin Advanced Imaging Laboratories, Duke University Medical Center, 2424 Erwin Road, Hock Plaza, Suite 302, Durham, North Carolina 27705

B. M. W. Tsui
The Russell H. Morgan Department of Radiology and Radiological Science, Johns Hopkins Medical Institutions, Baltimore, Maryland 21287

Purpose: The authors develop the 4D extended cardiac-torso (XCAT) phantom for multimodality imaging research.

Methods: Highly detailed whole-body anatomies for the adult male and female were defined in the XCAT using nonuniform rational B-spline (NURBS) and subdivision surfaces based on segmentation of the Visible Male and Female anatomical datasets from the National Library of Medicine as well as patient datasets. Using the flexibility of these surfaces, the Visible Human anatomies were transformed to match body measurements and organ volumes for a 50th percentile (height and weight) male and female. The desired body measurements for the models were obtained using the PEOPLESIZE program that contains anthropometric dimensions categorized from 1st to the 99th percentile for US adults. The desired organ volumes were determined from ICRP Publication 89 [ICRP, "Basic anatomical and physiological data for use in radiological protection: reference values," ICRP Publication 89 (International Commission on Radiological Protection, New York, NY, 2002)]. The male and female anatomies serve as standard templates upon which anatomical variations may be modeled in the XCAT through user-defined parameters. Parametrized models for the cardiac and respiratory motions were also incorporated into the XCAT based on high-resolution cardiac- and respiratory-gated multislice CT data. To demonstrate the usefulness of the phantom, the authors show example simulation studies in PET, SPECT, and CT using publicly available simulation packages.

Results: As demonstrated in the pilot studies, the 4D XCAT (which includes thousands of anatomical structures) can produce realistic imaging data when combined with accurate models of the imaging process. With the flexibility of the NURBS surface primitives, any number of different anatomies, cardiac or respiratory motions or patterns, and spatial resolutions can be simulated to perform imaging research.

Conclusions: With the ability to produce realistic, predictive 3D and 4D imaging data from populations of normal and abnormal patients under various imaging parameters, the authors conclude that the XCAT provides an important tool in imaging research to evaluate and improve imaging devices and techniques. In the field of x-ray CT, the phantom may also provide the necessary foundation with which to optimize clinical CT applications in terms of image quality versus radiation dose, an area of research that is becoming more significant with the growing use of CT. © *2010 American Association of Physicists in Medicine.* [DOI: 10.1118/1.3480985]

Key words: medical imaging simulation, computer phantom, SPECT, PET, CT

I. INTRODUCTION

With the advent of new imaging techniques and diagnostic methods in response to disease, a major challenge is how to evaluate which technique is best in terms of patient diagnosis and treatment and how these techniques may fit together to form a complete patient management strategy. It is essential for the advancement of emerging imaging systems to have a tool that can be used for technique testing, evaluation, and comparison. Each technique involves several selectable parameters for image acquisition, reconstruction, processing,

and analysis. It would not be feasible to test every combination of scanning parameters and every clinical task on patients under clinical conditions, especially for x-ray systems given the relatively high radiation dose. The use of physical phantoms is also limited in that it would be prohibitively expensive to fabricate a realistic range of patient sizes, variations, and deformations. Imaging simulation using computer generated digital phantoms offers a practical approach to evaluate and determine optimized imaging techniques.

In computer-based simulation, digital phantoms provide a virtual model of the patient's anatomy and physiology. Imaging data of a phantom can be generated as if it was a live patient using an accurate computerized model of the physics of the imaging process. With simulation, it is therefore possible to perform clinical experiments entirely on the computer. The advantage in using such studies is that the exact anatomy of the phantom is known, thus providing a "gold standard" or "truth" from which to evaluate and improve imaging devices and techniques. The user knows precisely what the simulated images should reveal in regard to such things as organ volumes or boundaries, tumor locations, sizes, shapes, extent and frequency of motion, etc. In order for simulation results to have merit, however, it is vital to have a 4D digital phantom that provides realistic models of human anatomy and cardiac and respiratory motions.

With their great potential in imaging research, much work has been done to create more realistic computerized phantoms. These typically fall into three general classes: Voxelized, mathematical, and the recently introduced hybrid phantoms. Voxelized phantoms, e.g., Ref. [1], are based on segmented patient data and, therefore, provide a realistic model of patient anatomy. Since they are fixed to a particular patient anatomy, though, it is difficult to model anatomical variations or motion with voxelized models. Mathematical phantoms, e.g., Ref. [2], define the organs and structures in the body using equations or simple geometric primitives. They are at the opposite side of the spectrum from voxelized phantoms. They are easily manipulated through the equations that define them to model variations in the organs or organ motion, but the simplicity of the equations upon which they are based limits their ability to realistically model the human anatomy. Hybrid phantoms have recently been introduced that seek to combine the advantages of voxelized and mathematical phantoms.[3,4] Hybrid phantoms are based on segmented patient data, but they use nonuniform rational B-splines (NURBS)[5,6] or polygon meshes to define each anatomical object. Based on patient data, the NURBS surfaces or polygon meshes can accurately model each structure in the body, providing the realism of a voxelized model. They also maintain the flexibility to model anatomical variations and motion. The NURBS surfaces are easily manipulated through the control points that define their shape, while the polygon meshes can be easily altered through the vertex points that define the polygons.

The 4D NCAT phantom[3,7,8] (Fig. 1), a hybrid phantom in our laboratory, was developed to provide a realistic and flexible anatomical model of the human torso for use in nuclear medicine research, specifically single-photon emission com-
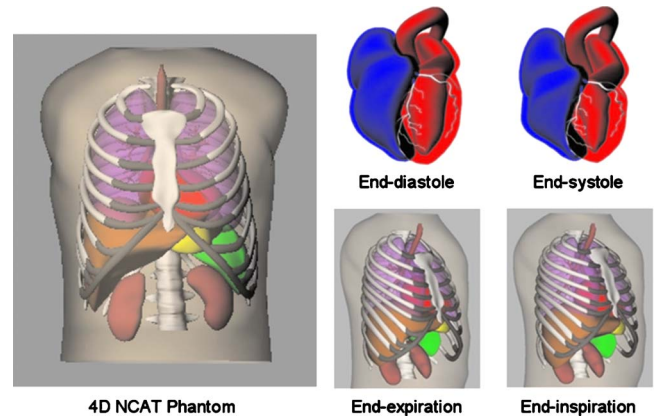

FIG. 1. (Left) Anterior view of the original 4D NCAT phantom. The NCAT includes models for the cardiac and respiratory motions. (Top right) Surface renderings of the cardiac model of the NCAT at end-diastole and end-systole. (Bottom right) Surface renderings of the NCAT at end-expiration and end-inspiration.

puted tomography (SPECT) and positron emission tomography (PET). NURBS surfaces were used to construct the organ shapes in the NCAT phantom using the Visible Human male CT data from the National Library of Medicine (NLM) (Ref. [9]) as their basis. Female NCAT anatomies were created by the addition of breast surfaces to the base male torso. The 3D NCAT phantom was extended to four dimensions to model common patient motions such as the cardiac and respiratory motions using 4D tagged magnetic resonance imaging (MRI) data and 4D high-resolution respiratory-gated CT data, respectively. Both datasets were acquired from normal male patient volunteers.

With its basis upon human data and the inherent flexibility of the NURBS primitives, the 4D NCAT phantom provides an ideal tool to simulate a patient or patient population in a simulation study to augment or potentially replace costly patient studies. Transformations can be applied to the base anatomy of the phantom to produce many different anatomical variations for research.[10] Combined with accurate models of the imaging process, the phantom can simulate imaging data from different modalities (Fig. [1]). The 4D NCAT has gained and continues to gain widespread use in nuclear medicine imaging research, especially for the design, evaluation, and improvement of imaging instrumentation, data acquisition techniques, and image processing and reconstruction methods. It has currently been distributed to more than 300 academic users around the world.

Despite its widespread use, the 4D NCAT phantom is limited by its original design. As mentioned above, the phantom only includes the torso region and does not include a separate model for the female anatomy. Also, the phantom, capable of being far more realistic, was designed specifically for lower resolution nuclear medicine imaging research.[11] It, therefore, lacks the anatomical detail for use in more high-resolution nuclear medicine and other high-resolution imaging modalities, such as x-ray CT and MRI.

In this work, we develop the next generation NCAT phantom, the 4D extended cardiac-torso (XCAT) phantom for
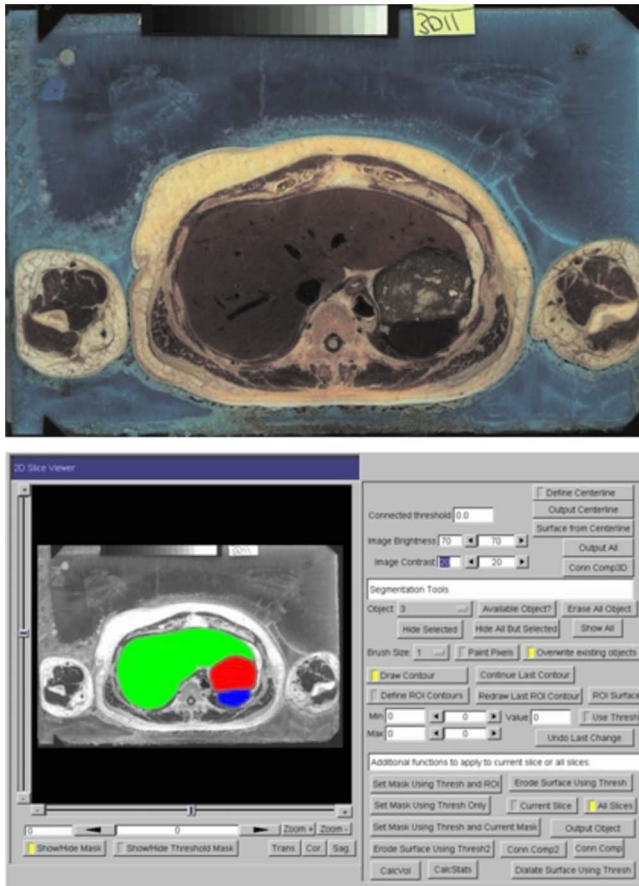
FIG. 2. (Top) Example slice from the Visible Female anatomical data from the NLM. The NLM data for the male and female were segmented to create the base anatomies for the XCAT phantom. (Bottom) Screenshot from the IMAGESEGMENT program used to segment the Visible Human data. The same slice of the Visible Female is shown with the liver, stomach, and spleen segmented.

multimodality imaging research to evaluate and compare imaging devices and techniques. The XCAT includes highly detailed whole-body male and female anatomies and improved models for the cardiac and respiratory motions based

on state-of-the-art high-resolution imaging data. With these vast improvements, the resulting 4D XCAT phantom is applicable to more medical imaging applications, spanning the entire range from low to high resolution.

II. MATERIALS AND METHODS

The 3D male and female anatomies of the XCAT were primarily based on the Visible Human anatomical data[9] distributed freely from the National Library of Medicine (NLM) (Fig. 2). The structures in the brain were created separately based on the existing MRI data of a normal subject. Models for the cardiac and respiratory motions were based on the existing gated 4D CT datasets obtained from normal subjects. All patient data were obtained in accordance with the standards of the Health Insurance Portability and Accountability Act (HIPAA). Each dataset was stripped of any identifying information and was therefore subject to exemption 4 from the Institutional Review Board (IRB). Table I summarizes the imaging data used to develop the XCAT phantom.

II.A. Development of the XCAT male and female template anatomies

The Visible Male dataset from the NLM consisted of 1878 transaxial anatomical slices over the entire body with a matrix size of 2058×1216 and an in-plane pixel size of 0.33 mm and a slice thickness of 1 mm. The female dataset was defined similarly except the slices were obtained at a slice thickness of 0.33 mm, resulting in over 5000 anatomical images over the entire body. Compared to CT data traditionally used to create computational phantoms, the anatomical images of the NLM provide a higher resolution especially in terms of the slice thickness. CT datasets usually have a slice thickness of 3–5 mm. The anatomical images are also actual color images of the body and provide better tissue contrast, especially for things such as the heart and liver which have similar attenuation characteristics and blend together in CT images.

TABLE I. Imaging data used to create the 4D XCAT phantom anatomies and motions.

| Data	Resolution	Use
Visible Human Male anatomical data	0.33 mm pixel width 1.0 mm slice thickness	Basis for male anatomy with the exception of the heart and brain
Visible Human Female anatomical data	0.33 mm pixel width 0.33 mm slice thickness	Basis for female anatomy with the exception of the heart and brain
4D cardiac-gated multislice CT data (male subject)	0.32 mm pixel width 0.4 mm slice thickness 100 time frames	Basis for male beating heart
4D cardiac-gated multislice CT data (female subject)	0.4 mm pixel width 0.6 mm slice thickness 12 time frames	Basis for female beating heart
3D MRI data (male subject)	0.9375 mm pixel width 1.0 mm slice thickness	Basis for male and female brain
4D respiratory-gated multislice CT data (male and female subjects)	0.89 mm pixel width 2.5 mm slice width	Basis for default respiratory motions for the organs
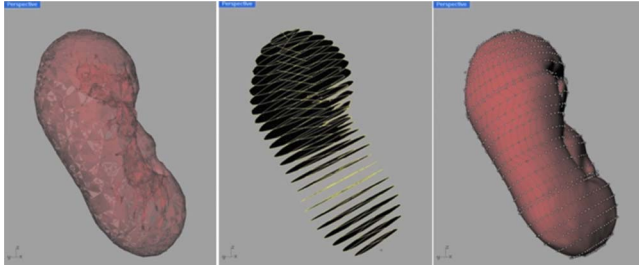
FIG. 3. Screenshots from the RHINOCEROS NURBS modeling program used in this example to define a NURBS surface for the kidney. To define an organ as a NURBS surface, a 3D polygon model created from segmentation is read into the program (left). Contours are then taken from the polygon model (middle). A 3D NURBS surface is then fit to the contours (right). The shape of the NURBS surface can be modified by manipulating its control points (open squares).

FIG. 4. Gated MSCT cardiac data with the heart at (left) end-diastole and (right) end-systole. The male heart is shown as example.

Using a tablet PC, the anatomical structures for the male and female were segmented using the manual, automatic, and semiautomatic segmentation functions of IMAGESEGMENT, a custom graphical application developed in our laboratory (Fig. 2). IMAGESEGMENT allows a user to skip slices in the segmentation process. Interpolation is performed between contoured slices using cubic spline surfaces. This ability greatly speeds up the analysis of the datasets as every slice does not need to be individually segmented. Within the framework of IMAGESEGMENT, each segmented structure was converted into a 3D polygon model using the marching cubes algorithm from the visualization toolkit (VTK) (www.vtk.org).

Cubic NURBS surfaces were used to model every structure except the brain, which was based on a separate set of patient data as described below. NURBS surfaces are advantageous over polygon meshes in that they can model objects using a smaller number of parameters. While a polygon mesh of an object may contain tens of thousands of vertices, a NURBS surface may model the same object with the same level of accuracy using just 10–200 control points. They, therefore, provide a more compact mathematical description for an object. The polygon models were input to the RHINOCEROS NURBS modeling software,[12] which allows a user to visualize and manipulate models in 2D and 3D (Fig. 3). The 3D NURBS surfaces were optimally fit to each model using tools within RHINOCEROS. Separate surfaces were created for each bone, muscle, blood vessel, and airway tree branch defined by segmentation.

Due to some distortion of the brain structures in the Visible Human data, the brain was modeled separately based on MRI data of a normal male subject. The data were $256 \times 256 \times 141$ with a pixel width of 0.9375 mm and a slice thickness of 1.0 mm. The brain structures were segmented and converted into 3D polygon models as before; however, subdivision (SD) surfaces (Ref. 13) were used to define the models instead of NURBS due to their ability to more efficiently represent structures of arbitrary topological type such as the white and gray matter in the brain. To model such objects using NURBS would require partitioning the object into a collection of individual overlapping NURBS surfaces,
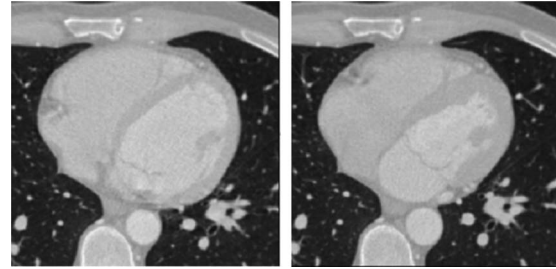
which would introduce a larger combined number of control points to define the model. This would minimize or eliminate the advantage of NURBS over polygon meshes. So in this case, it was best to just have one model for each object defined as a polygon mesh. Each polygon model for the brain was used as the initial mesh representation for a SD surface. The SD surfaces can be iteratively subdivided and smoothed using a refinement scheme[14] to produce smooth surfaces. The SD brain model was scaled within RHINOCEROS to fit the male and female Visible Human XCAT anatomies.

In creating the anatomies for the 3D XCAT, some peculiarities were fixed manually. It was found that the Visible Male was missing the left testicle. This was added using the right testicle as a guide. The transverse colon of the Visible Female was found to descend far into the pelvis before ascending back up to join the descending colon. This surface was adjusted using the Visible Male as a guide. The arms were adjusted in both anatomies to lie by their sides. Originally, they were folded across the chest.

For both the male and female anatomies, the airway tree in the lungs was extended using the physiologically based mathematical algorithm described in Ref. 15. Using this algorithm, the initial airway tree model (approximately four generations) obtained from segmentation was extended to 16 generations based on optimally distributing the flow through the available lung space.

II.B. Incorporation of a 4D cardiac model

High-resolution cardiac-gated MSCT data obtained from healthy male and female subjects (Fig. 4) was used to create more detailed cardiac models for the XCAT phantom. One set of data was used for each gender. The male study included 100 total time frames over a complete cardiac cycle with a pixel size of 0.32 mm and a slice thickness of 0.4 mm. The female dataset was not as temporally detailed, containing only 12 time frames with a pixel size of 0.4 mm and a slice thickness of 0.6 mm. The gated data were obtained with the subjects at rest.

To create each heart model, we first segmented the CT data for each time frame. For the male dataset, all 100 time frames were not needed to capture the beating heart motion. We, therefore, segmented every fifth frame for a total of 20 time points over the cardiac cycle. For the female dataset, we

segmented all 12 frames. The heart chambers (left and right ventricles and atria) were segmented from each frame and converted into 3D polygon models using the IMAGESEGMENT program. 3D NURBS surfaces were then fitted to the polygon models defining each heart structure using the RHINOCEROS 3D NURBS modeling software.[12]

The time correspondence between control points defining each surface over the time frames was set up using the original 4D NCAT cardiac model based on tagged magnetic resonance imaging (MRI) data.[3] This model accurately represents the contracting, twisting motion of the heart that has been previously described using tagged MRI analysis.[16] The twisting motion of the heart could not be ascertained from CT imaging data; therefore, the cardiac twist illustrated in the 4D NCAT was scaled to fit the new heart geometry segmented from the CT data. Each control point of the CT-based left ventricle (LV) model at end-diastole was defined in terms of its distance from the base of the ventricle, its angular position about the center of the LV, and its distance from the endocardial surface. The distance values were normalized to range from 0 to 1, while the angles ranged from 0° to 360°. For a given control point, these values were used to find the corresponding location within the NCAT heart. The twisting motion for the NCAT defined at this point was then applied to the control point of the CT-based LV to define its angular position at subsequent frames. The right ventricle (RV) was handled in a similar fashion. Once the twisting motion was established, the radial and longitudinal contractions of the control points could be obtained by noting the epi- and endocardial borders in the gated MSCT images. Using this technique, the 3D position of each control point defining a cardiac surface was determined for each time frame. Time curves were then defined for each control point's position creating a time changing 3D surface or 4D NURBS model for each heart chamber.

In addition to the cardiac chambers, the coronary artery tree and other vessels of the heart were modeled. Initial 3D NURBS surface models were created by segmenting the initial time frame of the gated MSCT data. The motion of the different structures throughout the cardiac cycle was determined by tracking landmark points located on or within them for each subsequent time frame. For example, to determine the motion of the coronary vessels, we tracked the branching points at which the vessels divide. From the motion analysis, we created dynamic NURBS models for the heart structures using the 4D NURBS technique previously used to create the initial cardiac and respiratory models of the NCAT phantom.[3,7,8] Based on the motion of the landmark points, time curves were derived for the 3D position of the control points that define the different structures creating a 4D NURBS model.

The 4D NURBS surfaces for the coronary artery tree and heart valves were incorporated with those created for the cardiac chambers to create more realistic and detailed cardiac models for the XCAT phantom. The heart models were set up so that through modification of parameters (ejection fraction, longitudinal and radial contraction, cardiac twist, heart rate, etc.) that define them, they are capable of modeling a wide variety of beating heart motions, normal and abnormal.[17] Table II lists the different parameters that control the cardiac motion as well as parameters that can alter the anatomy of the phantom and its respiratory motion.

The heart models were incorporated into the new XCAT male and female anatomies. Using the RHINOCEROS program, the NURBS-based hearts (defined at the end-diastolic phase) were manually translated, rotated, and scaled to optimally fit within the bodies using the segmented Visible Human hearts as a guide (Fig. 5). In placing the NURBS-based hearts in the body, the aorta, superior vena cava, inferior vena cava, and pulmonary vessels were matched up closely to those of the Visible Human anatomies. The vessels were then connected to those in the body. This required little work as the hearts were found to match up very well with their Visible Human counterparts. The surfaces for the lungs were sculpted to accommodate the new pericardium surfaces. The placement of the hearts within the Visible Human anatomies did not alter the beating heart motion of each model. The hearts contract and twist as they were originally set to do. However, the beating heart motion does slightly affect the neighboring lungs as described in Sec. II C.

II.C. Modeling respiratory mechanics

The original 4D NCAT phantom included a flexible, parametrized respiratory model based on respiratory mechanics[8] and an analysis of sets of respiratory-gated CT data of normal subjects.[18] Briefly, the respiratory motion is controlled by two time curves, one defining the change in the diaphragm height and one defining the amount of anterior-posterior (AP) expansion of the chest. These curves can be input by the user to model different types of breathing. By default, they are set up as shown in Fig. 6.

The respiratory mechanics of the new 4D XCAT male and female were set up to work in the same manner. Given a time point in the respiratory cycle, the ribcage is set up to rotate upward and outward to expand the chest by the amount defined by the AP curve. The diaphragm is set up to contract downward by the amount specified by the diaphragm curve and forward according to the AP curve. The heart, liver, stomach, spleen, and kidneys all move with scaled down motions from that of the diaphragm according to user-defined parameters. The motion of these organs and the ribcage are used to set up a motion vector field (MVF) from which to define the motion of the other structures that move during respiration (abdominal organs, organ vessels, and muscle tissue) (Fig. 7). The MVF is created by voxelizing the chest and abdomen regions of the XCAT anatomy (5 mm isotropic resolution) with integer IDs defined for each structure and assigning fixed vectors for each organ that moves with a defined motion. The vectors are fixed to zero for structures that do not move such as the backbone, pelvis, and rectum. The vectors for the remaining voxels in the body (defining the abdominal organs, muscle, etc.) are initially set to zero. The MVF is then smoothed until these vectors become stable (change is less than a specified tolerance value). For each smoothing iteration, the vectors are checked and

TABLE II. Anatomical and motion parameters of the XCAT phantom.

Anatomical parameters	
X, Y, and Z scaling factors for the phantom	One-dimensional scaling factors applied to the entire phantom
X, Y, and Z scaling factors for the head, chest, abdomen, and pelvis	One-dimensional scaling factors for the different regions of the body—scales everything in the different regions
X, Y, and Z scaling factors for the head, chest, abdomen, and pelvis skin layers	One-dimensional scaling factors for the outer skin of the different regions of the body—scales only the skin
Arm and leg circumference	Radial scaling factors for the arms and legs—scales everything in the regions
Arm and leg skin circumference	Radial scaling factors for the outer skin of the arms and legs—scales only the skin
Arm and leg lengths	Scales the lengths of the arms and legs—scales everything in the arms and legs
Bone scaling	Scales all bones in 2D about their centerlines, makes each bone bigger or smaller
Bone thicknesses	Sets the thickness of the different bones
Muscle scaling factors for the head, torso, arms, and legs	Compresses/expands the muscles in the different regions
Heart scale	Scales the heart in 3D
X, Y, and Z translations and rotations for the heart	Sets the position of the heart in the body
Height of diaphragm/liver dome	Sets the height of right and left diaphragm
Volume parameters for the organs	Sets the volumes of the different organs
Cardiac motion parameters	
Heart period	Sets the length of the beating heart cycle
Left ventricle (LV) volume parameters	Sets the LV volumes at end-diastole, end-systole, at the beginning of the quiet phase, at the end of the quiet phase, and during reduced filling
Cardiac cycle timing parameters	Sets the duration from end-diastole to end-systole, the duration from end-systole to the beginning of the quiet phase, the duration from the beginning to the end of the quiet phase, and the duration from the end of the quiet phase to reduced filling
Parameters to define a perfusion defect in the left ventricle	Sets the size and location of a perfusion abnormality in the LV; motion of the defect can be scaled up or down using a scaling factor
Parameters to define a plaque in the coronary vessels	Sets the size and location of a plaque in the coronary arteries
Respiratory motion parameters	
Respiratory period	Sets the length of the respiratory cycle
Anterior-posterior expansion	Sets the extent in cm's of the anterior-posterior expansion of the chest. This is done by scaling the anterior-posterior respiratory time curve (Fig. 6)
Diaphragm motion	Sets the extent in cm of the diaphragm motion. This is done by scaling the diaphragm time curve (Fig. 6)
Diaphragm curve	Name of curve that controls the diaphragm motion during respiration. User can define their own using the default (Fig. 6) as a guide
Anterior-posterior expansion curve	Name of curve that controls the anterior-posterior motion during respiration; user can define their own using the default (Fig. 6) as a guide
Heart respiratory motion translations	Sets the x, y, and z extents in cm of the heart's motion during breathing
Heart respiratory motion rotations	Sets the extents in degrees of the x, y, and z rotations of the heart during breathing
Parameters to define a spherical lesion in the body	Sets the size and location of a spherical lesion in the body; lesion will move with the respiratory motion

corrected to make sure that structures do not run into each other. The vectors are checked by following their path in the voxelized field. If they are found to intersect voxels of fixed objects as determined from the integer IDs, the vectors are modified so their ending point is three-quarters the distance to the intersection. Once the MVF is set, the control points
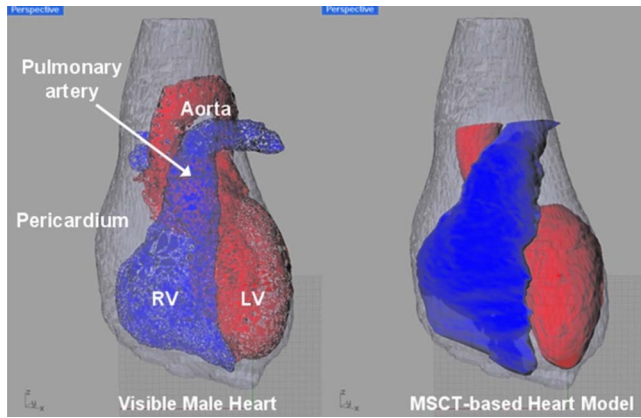
FIG. 5. (Left) Segmented surfaces (pericardium, aorta, pulmonary artery, and left and right ventricles) from the Visible Male heart as displayed in RHINOCEROS. (Right) MSCT-based heart model transformed to fit within the Visible Human. Surfaces for the LV and RV and the initial aorta and pulmonary artery of the MSCT-based model are shown over the transparent pericardial surface of the Visible Human to illustrate the degree of fit.

FIG. 7. Motion vector field transforming the XCAT from end-expiration to end-inspiration. The vector magnitudes are shown in the above image with larger motions indicated by darker intensities. The majority of the motion occurs at the diaphragm. The motion tails off from there in a very smooth fashion.

defining each organ and structure in the phantom are located within the field to determine their motion at the given time point. By applying the vectors to the control points, the organs deform with the respiratory motion. The total process to determine the motion of the organs takes only a few seconds per frame. All of these take place within the XCAT phantom software. If a user wants to output a time series of phantoms over the respiratory cycle, the above process is done to create each phantom at each time frame.

The XCAT respiratory motion was parametrized like it was for the NCAT (Table II). Users can control the breathing rate, the amount of diaphragm motion, the amount of chest expansion, and the amount of cardiac motion due to breathing. The diaphragm motion and chest expansion impact how much volume change there is in each lung. By changing these parameters, different levels of breathing can be simulated from quiet to heavy breathing. The motions of the different organs and diaphragm are initially set to default values for tidal breathing. These values were determined from an

analysis of 20 sets of 4D respiratory-gated CT data of normal subjects.[18] Each dataset contained 10 frames over the respiratory cycle with the patient breathing normally. We segmented the data for each time frame for each patient and then compared the structures over time visually using the RHINOCEROS program. From this analysis, we assessed how the structures changed over the respiratory cycle. We then determined the range in motion about the different directions for the organs. We set the phantom defaults to the average motion observed for each organ.

II.D. Interaction between the cardiac and respiratory motions

The cardiac and respiratory motions are set up to interact with one another in the XCAT phantom. As discussed above, the heart will move up and down with the motion of the diaphragm during breathing. In terms of the cardiac motion and its affect on the lungs, this is handled using a motion vector field of the heart and lung region with vectors assigned for the heart structures. The vectors define the cardiac motion from the previous frame to the current one. For objects that do not move, the vectors are fixed to zero. The vectors for the remaining voxels in the body (defining the abdominal organs, muscle, etc.) are initially set to zero. The MVF is smoothed and checked as it was for the respiratory motion. The control points defining the lung structures are then located within the field to determine their motion at the given time point.

II.E. Modeling 50th percentile anatomies

The Visible Male and Female represent the anatomies of larger individuals, the Visible Male being 1803 mm tall weighing approximately 100 kg (73rd and 85th percentile, respectively) and the Visible Female being 1650 mm tall weighing approximately 92 kg (63rd and 98th percentile, respectively). Using the flexibility of the NURBS and SD surfaces, the Visible Human anatomies were transformed to
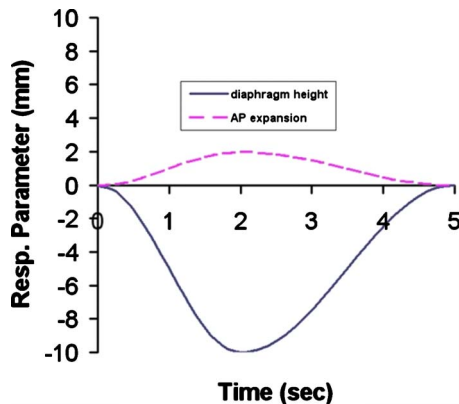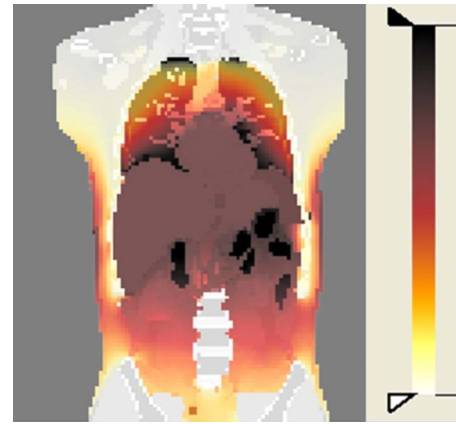

FIG. 6. Parameter curves for the NCAT phantom over the respiratory cycle. The default breath is set up to last 5 s with inspiration and expiration lasting 2 and 3 s, respectively. These curves can be adjusted by the user to simulate different breathing patterns.

TABLE III. PEOPLESIZE measurements for 25th, 50th, and 75th percentile US adult males and females.

Measurement	25% male	50% male	75% male	25% female	50% female	75% female
Height (mm)	1713	1761	1848	1586	1627	1712
Weight (kg)	70	81	92	58	66	78
Head circumference (mm)	574	585	597	536	547	558
Chest width at level of nipples (mm)	329	347	365	290	307	325
Waist width (mm)	287	303	319	238	265	291
Hip breadth (mm)	314	328	341	306	322	338
Chest depth at level of nipples (mm)	218	228	238	252	270	303
Waist depth (mm)	220	234	249	191	209	232
Trunk depth at buttocks (mm)	a	a	a	232	253	281
Upper arm circumference (mm)	304	328	355	270	298	333
Thigh circumference (mm)	561	601	646	588	625	684

[a]PEOPLESIZE did not have a value for this measurement; the trunk was scaled with the waist in this instance.

match body measurements and organ volumes for a 50th percentile (height and weight) male and female. The desired body measurements for 50th percentile subjects were obtained using the PEOPLESIZE program (http://www.openerg.com/psz/index.html), which contains anthropometric dimensions categorized from 1st to the 99th percentile for nine nationalities: American, Australian, Belgian, British, Chinese, French, German, Japanese, and Swedish. For our purposes, we used the survey data for US adults, ages 18–64. Table III lists the measurements used to tailor the male and female XCAT anatomies.

The desired organ volumes were determined from ICRP Publication 89.[19] As was done with the original NCAT, the XCAT phantom anatomies were parametrized to control body measurements (including height, head, chest and waist dimensions, and arm and leg circumferences) and organ volumes through 1D, 2D, and 3D scaling operations applied to the control points of the NURBS surfaces and the vertex points of the SD meshes (Table II). In changing a parameter, the phantom surfaces were set up to interact with one another using a collision detection so as to avoid structures protruding into one another. Each organ is defined with a backbone structure running through its center. Spokes are set up to radiate from this structure to the control points defining each organ model. When an organ is modified, collision with another object is automatically checked along each spoke using a Bezier clipping[20,21] algorithm to look for intersections along the path of the spoke. In this system, the organs in the phantom are defined with a priority system. If, when modeling an anatomical variation, an organ of higher priority is found to collide or overlap with one of lower priority, the lower priority organ is modified so as to eliminate the overlap. As a result, a lower priority organ will only change as much as it can without affecting higher priority organs.

Using the anatomical parameters, the male and female XCAT anatomies were optimally adjusted to create 50th percentile subjects. The organ masses were modified to be within 5% of the ICRP values. Figure 8 shows the transformation of the male phantom as displayed in RHINOCEROS. Each anatomy was visualized within RHINOCEROS to check for anatomical accuracy. The 50th percentile anatomies serve as standard templates from which users can create many different subjects through the phantom's anatomical parameters.

II.F. Pilot simulation studies

Like the original NCAT phantom, the new XCAT phantom can be combined with simulation tools modeling the different imaging modalities to produce realistic patient-quality images. Many excellent simulation packages in SPECT/PET,[22–24] MRI,[25,26] CT,[27,28] and ultrasound[29,30] already exist, which can take advantage of the phantom. As indicated by the referred articles, these packages have already been carefully validated to represent the actual performance of the image formation and data acquisition processes for multiple scanners. To demonstrate the potential of the 4D XCAT to produce realistic multimodality imaging data, we
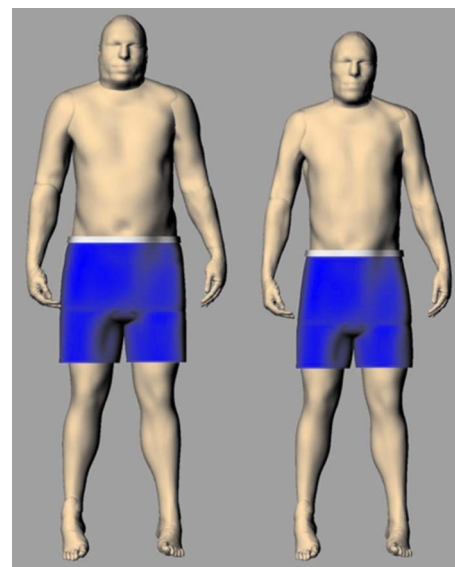

FIG. 8. (Left) Original body surfaces from the Visible Male. Using measurements from the PEOPLESIZE anthropometry database, the Visible Male body was transformed into that of a 50th percentile male adult (right).

utilized some of these simulation tools to generate PET, SPECT, and CT data over different regions of the body as described below.

II.F.1. ^{11}C-raclopride PET brain imaging

The structures in the XCAT male brain were assigned uptake ratios to model the distribution of ^{11}C-raclopride based on an analysis of patient data. A combination of two well-validated Monte Carlo codes, SimSET (Ref. 31) and GATE (Ref. 22), was used to generate the imaging data modeling the design parameters and the geometry of the second generation ECAT high-resolution research tomograph (HRRT) scanner.[32] Ninety-six projections were simulated then reconstructed using the ordered-subset expectation maximization algorithm[33] (24 subsets) with a pixel width and slice thickness of 1.2 and 3 mm, respectively.

II.F.2. In-111 ProstaScint® SPECT abdominal imaging

The abdominal anatomy of the male XCAT phantom was set to include such details as air pockets and/or activity in different sections of the intestines along with pelvic and abdominal lymph nodes so as to allow for the simulation of realistic background activities and lesions in the phantom. The distribution of radioactivity in the organs and structures was set to model the uptake of a typical indium 111 (In-111) ProstaScint® SPECT patient study based on an analysis of a large patient imaging database. Projection data were generated from the phantom using a combination of SimSET (Ref. 31) and an analytic projector developed in our laboratory that included the effects of photon attenuation, the full collimator-detector response including the geometric, penetration and scatter components, and scatter within the phantom.[34,35] Hot lesions were simulated in the obturator, external iliac, and common iliac nodes. Poisson noise was simulated in the projection data to obtain a count level roughly equivalent to that of a typical clinical study. The data were reconstructed with a pixel width and slice thickness of 0.69 mm using the conventional filtered backprojection (FBP) algorithm with the Butterworth filter at five cutoffs.

II.F.3. X-ray CT chest imaging

To illustrate the potential of the new 4D XCAT phantom to produce realistic high-resolution imaging data, x-ray CT images of male and female versions of the phantom were simulated. To efficiently simulate high-resolution CT images, we previously developed a unique analytic projection algorithm (including quantum noise) that accurately models the CT imaging process.[28] The analytical projection algorithm was used to produce CT projection data from the different male and female versions of the phantom. The 512×512 projection images were generated using the analytical CT projection algorithm with a parallel geometry and a standard x-ray energy spectrum with a tube voltage of 120 kVp and 5 mm aluminum filtration obtained from the Catalogue of Spectral Data for Diagnostic X Rays.[36] The projection data were reconstructed into CT images using the FBP algorithm.
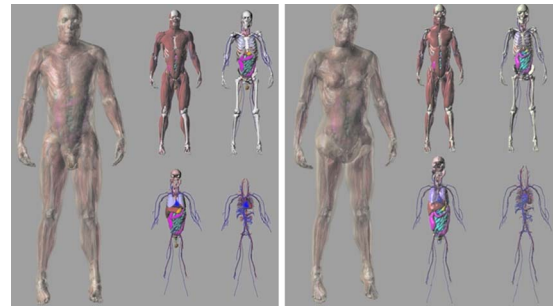
FIG. 9. 50th percentile male (left) and female (right) whole-body anatomies of the XCAT phantom. Different levels of detail are shown building up to the whole model for each, shown with transparency. The circulatory system, organs and glands, skeleton, and muscles are shown for both male and female.

For gated cardiac simulations, iodine contrast was modeled in the blood of the heart to better show the four chambers.

III. RESULTS

III.A. 4D XCAT anatomy and motion models

The original NCAT phantom (Fig. 1) consisted of only 100 structures restricted to the region of the torso. The new XCAT male and female are much more detailed including thousands of anatomical objects defined over the entire human body (Figs. 9 and 10). Table IV lists all the tissues defined in the XCAT phantom. Bone marrow was not segmented from the Visible Human data. Marrow (active plus inactive) is currently modeled as an inner surface to the bones. The thicknesses of the different bones can be specified by the user based on an analysis of patient data. Given the thickness value for a bone, the phantom program generates an inner surface for it. The space between the bone surface and the inner surface is defined as bone, whereas the space within the inner surface is defined as marrow. This gives the bone a uniform thickness. Fat is not explicitly modeled in the phantom. It is currently defined as the background tissue that is not classified as any other structure or tissue.

Table V shows the masses (g) of selected tissues defined in the XCAT (original Visible Human models as well as the 50th percentile phantoms) as compared to the ICRP adult male and female. The last two columns show the ratio of the
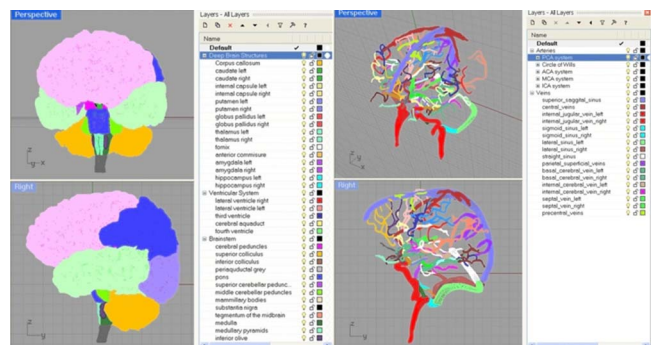

FIG. 10. Structures (left) and vessels (right) of the XCAT brain model.

TABLE IV. List of defined structures in the XCAT phantoms.

Brain	Heart	Skeleton	Remaining structures
Lateral ventricle	Pericardium	Bone marrow[a]	Adrenals
Third ventricle	Left atrium	Cervical vertebrae	Arteries and veins in the body
Fourth ventricle	Left ventricle	Thoracic vertebrae	Bladder
Cerebral aqueduct	Right atrium	Lumbar vertebrae	Body
Corpus callosum	Right ventricle	Vertebral disks	Diaphragm
Caudate	Atria and ventricular myocardium	Ribs	Ejaculatory ducts[b]
Internal capsule	Papillary muscles	Cartilage	Epididymus[b]
Putamen	Right coronary artery	Sternum	Esophagus
Globus pallidus	Left anterior descending coronary artery	Pelvis	Eyes
Thalamus	Left circumflex artery	Sacrum	Fallopian tubes[c]
Fornix	Coronary vein	Skull	Fat[d]
Anterior commissure	Pulmonary arteries and Veins	Mandible	Gall bladder
Amygdala	Superior vena cava	Teeth	Large intestine
Hippocampus	Inferior vena cava	Scapula	Larynx
Mamillary bodies	Aorta	Clavicle	Lens
Cerebral peduncles		Humerus	Liver
Superior colliculus		Radius	Lungs
Inferior colliculus		Ulna	Muscle
Periacquaductal gray		Bones in hand and fingers	Ovaries[c]
Pons		Femur	Pancreas
Superior cerebellar peduncle		Tibia	Parathyroid
Middle cerebellar peduncle		Fibula	Penis[b]
Substantia nigra		Patella	Pharynx
Medulla		Bones in foot and toes	Pituitary
Medullary pyramids			Prostate[b]
Inferior olive			Salivary glands
Tegmentum of midbrain			Seminal vesicles[b]
Midbrain			Small intestine
Cerebellum			Spinal cord
Frontal lobe			Spleen
Parietal lobe			Stomach
Temporal lobe			Testes[b]
Occipital lobe			Thymus
Grey matter			Thyroid
White matter			Trachea and bronchi
Anterior cerebral artery			Ureter
Middle cerebral artery			Urethra
Posterior cerebral artery			Uterus[c]
Internal cerebral artery			Vagina[c]
Circle of Wills			Vas deferens[b]
Veins			

[a]Bone marrow is modeled as interior surfaces within the bones; thickness of bones can be set in the phantom program.
[b]Male version only.
[c]Female version only.
[d]Fat is currently defined as the background tissue in the body not classified as anything else.

50th percentile masses to the ICRP values. They are all within ±5% with the exception of the lungs. The lungs are defined at end-expiration and their volumes can be adjusted by simulating respiratory motion.

In addition to the base anatomies, the cardiac and respiratory motions of the 4D XCAT are also much more detailed, as shown in Fig. 11. The heart model has been completely redone and includes more detailed structures for the cardiac chambers and includes the vessels and papillary muscles. The XCAT heart is much more realistic than that of the original NCAT (Fig. 1). The respiratory motion of the XCAT is based on similar mechanics to that of the NCAT, but it now includes the motion of the pulmonary vessels and muscles.

III.B. Simulation of realistic 3D and 4D multimodality imaging data from the XCAT

Figure 12 shows some sample slices of ^{11}C-raclopride PET, In-111 ProstaScint® SPECT, and chest CT data simulated from the male XCAT phantom. The simulated images compare very favorably to actual patient data. This demonstrates the great potential the XCAT has in imaging research.

TABLE V. Masses (*g*) of organs and tissues of the XCAT adults versus ICRP values.

Tissue	XCAT Visible male	XCAT Visible female	50% male XCAT	50% female XCAT	ICRP male	ICRP female	XCAT 50% male/ICRP	XCAT 50% female/ICRP
Adrenals	14.2	13.9	14	13	14	13	1	1
Bladder	87.6	31	51	40	50	40	1.02	1
Brain	1 361	1 386	1 420	1 290	1 450	1 300	0.98	0.99
Breasts[a]	–	1 082	–	525	25	500	–	1.05
Epididymus	2.5	–	4	–	4	–	1	–
Esophagus (wall)[b]	43	39	40	35	40	35	1	1
Eyes	14.7	15	14.8	15	15	15	0.99	1
Eyes (lens)	0.4	0.42	0.4	0.4	0.4	0.4	1	1
Fallopian tubes	–	1.4	–	2.1	–	2.1	–	1
Gall bladder (total)[b]	31.2	50	69	55	68	56	1.01	0.98
Heart (total)	910	850	830	610	840	620	0.99	0.98
Kidneys (2)	348	320	316	271	310	275	1.02	0.99
Large Intestine (wall)[b]	464	391	370	360	370	360	1	1
Larynx	17.8	15	27.9	19	28	19	1	1
Liver	1 861	2 250	1 820	1 354	1 800	1 400	1.01	0.97
Lungs[c]	1 100	810	1 066	875	1 200	950	0.89	0.92
Ovaries	–	1.9	–	11	–	11	–	1
Pancreas	90.4	90	135	119	140	120	0.96	0.99
Pituitary	0.62	0.61	0.6	0.6	0.6	0.6	1	1
Prostate	19	–	17.5	–	17	–	1.03	–
Salivary glands	102.8	65	81	68	85	70	0.95	0.97
Small Intestine (wall)[b]	772	1000	640	600	640	600	1	1
Spleen	238	155	153	125	150	130	1.02	0.96
Stomach (total)[b]	457	910	402	360	400	370	1.01	0.97
Testes	37.7	–	36	–	35	–	1.03	–
Thymus	14.2	23	26	21	25	20	1.04	1.05
Thyroid	27.8	17.5	19.7	17	20	17	0.99	1
Trachea	5.7	8.1	10	8	10	8	1	1
Ureters	15.3	14.2	15	15	16	15	0.94	1
Uterus	–	55	–	83	–	80	–	1.04
Bone (total)	6 300	4 700	5 700	4 200	5 500	4 000	1.04	1.05
Marrow	4 300	2 682	3 500	2 600	3 650	2 700	0.96	0.96
Muscle	39 000	18 300	30 500	17 000	29 000	17 500	1.05	0.97
Body (total)	100 000	92 000	73 600	62 300	73 000	60 000	1.01	1.04

[a]Not currently separated from the male chest surface.
[b]Organ content and wall volumes are adjustable within the phantom program.
[c]Lung volumes are dependent on the breathing motion; here they are defined at end-expiration.

With its extension to the abdomen and head, it can be applied to more research applications in nuclear medicine such as techniques for brain imaging or for imaging of prostate, ovarian, or cervical cancer. With the enhanced anatomical detail, it can be used for research in high-resolution imaging such as high-resolution PET, x-ray CT, or MRI. The phantom is also capable of being used for dual modality imaging systems such as SPECT-CT or PET-CT.

Figure 13 shows CT images simulated from three adult male patients of different body sizes using the XCAT phantom. Body measurements (width and depth of the chest, abdomen, and pelvis) for a 25th and 75th percentile male adult, in terms of weight, were obtained using the PEOPLESIZE program (Table III). The XCAT parameters were then adjusted so that the phantom measurements would match up to the corresponding values from PEOPLESIZE, creating new phantoms for a 25th and 75th percentile male. For each case, the phantom height and the interior organ anatomy were not changed. As can be seen in the images, the outer body surface shrinks and expands around the constant interior anatomy with the body changing the most in the abdominal region of the body (the area where there are the least structures repelling the body change). Through this example, the XCAT can be seen to have a great deal of flexibility. It is not limited to a single set of anatomies. Through various user-defined parameters, it can be used to simulate any number of anatomically diverse subjects. As such, it can provide a vital tool to investigate the effect of anatomy in CT imaging. Various scanning parameters can be altered and their effects can be witnessed on anatomically variable subjects. Through such studies, one can devise patient specific imaging protocols so as to reduce radiation dose while maintaining a diagnostic image quality.

With the improved anatomical detail of the cardiac and respiratory motion models, the XCAT can also produce more realistic simulated 4D imaging data. Figure 14 shows 4D
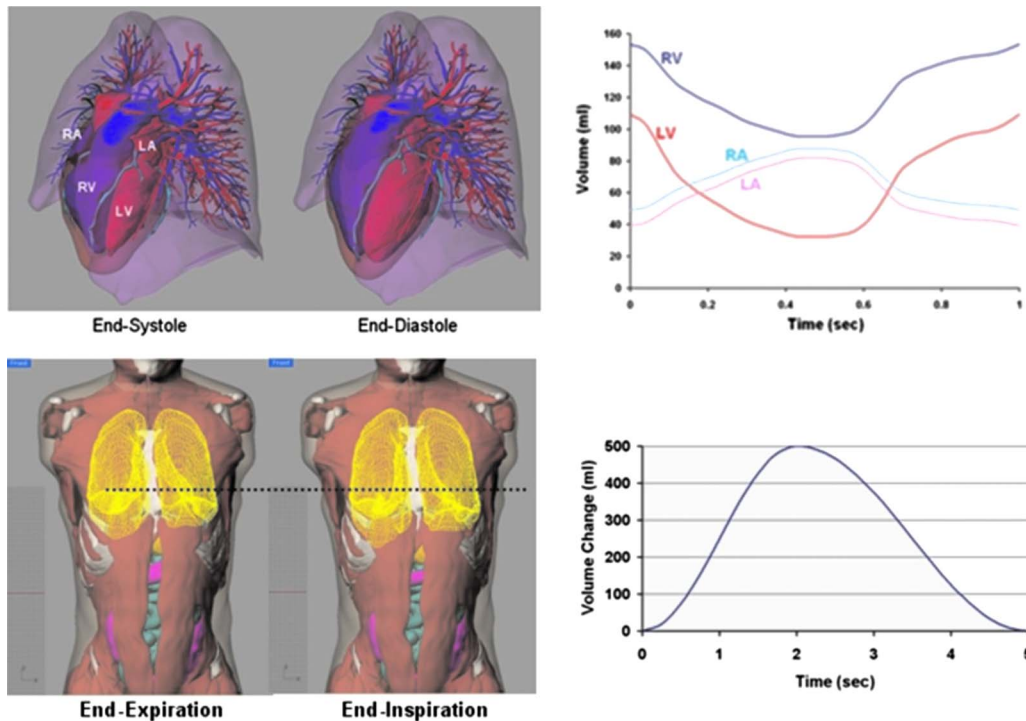
FIG. 11. Enhanced motion models of the 4D XCAT, male shown as example. (Top) XCAT cardiac model based on MSCT. Plots of the volume change in the cardiac chambers, LV, RV, left atrium, and right atrium for the default motion are shown to the right. (Bottom) XCAT respiratory model based on respiratory-gated CT. The lungs are highlighted within the body. Dotted line indicates the height of the right diaphragm. Plots of the volume change in the lungs are shown to the right.

cardiac- and respiratory-gated CT simulated images simulated from the female XCAT. Both motion models are parametrized so as to simulate many different normal and abnormal variations. With this ability, the phantom is a great resource to investigate the effects of motion on medical imaging and to develop compensation methods for these effects.

IV. DISCUSSION

As demonstrated above, the 4D XCAT phantom developed in this work can realistically model the complex shapes of real human organs and has the flexibility to model ana-
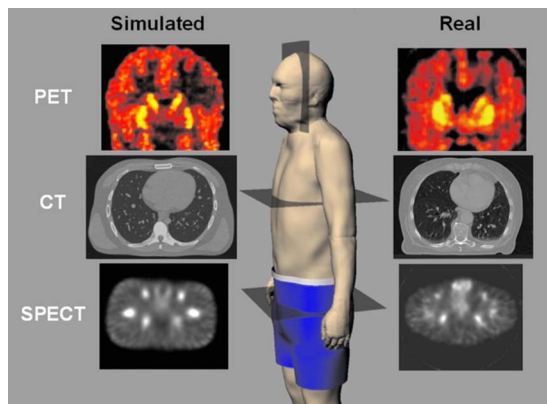

FIG. 12. Imaging simulations performed using the XCAT phantom. PET (top), CT (middle), and SPECT (bottom) images are shown. Image planes of the reconstructed images are shown on the phantom model.

tomical variations and motion. It offers a vast improvement over its NCAT predecessor including highly detailed whole-body male and female anatomies containing thousands of defined structures as well as enhanced models for the cardiac and respiratory motions.

Combined with accurate models of the imaging process, the XCAT can produce realistic multimodality imaging data close to that obtained from patient studies. With its improved anatomical detail and whole-body definition, it is applicable to more medical imaging applications using modern high-resolution imaging modalities and techniques. Through user-defined parameters, any number of different anatomies, cardiac or respiratory motions or patterns, and spatial resolutions can be simulated to perform medical imaging research.

Despite these abilities, the 4D XCAT phantom still suffers from some limitations. Each tissue modeled is defined as a homogeneous composition. In future work, we will investigate techniques to model tissue heterogeneity within each organ using methods similar to those used to characterize breast structure in mammograms. We are also investigating moving toward finite-element (FE)-based modeling for inter-organ interactions and motion. Currently, these interactions are handled using the motion vector fields described in Sec. II. The vector fields do not consider the different material properties of the tissues and how they would interact due to induced changes. FE techniques would provide a more physiological basis for the phantom and these interactions. FE modeling would also allow for more flexibility in that

FIG. 13. CT data simulated using the 25th, 50th, and 75th percentile (weight) male XCAT phantoms. Coronal, sagittal, and transaxial slices are shown for each.

FIG. 14. Cardiac-gated (top) and respiratory-gated (bottom) CT images generated using the 4D female XCAT.

more physiologically based parameters (cardiac remodeling, blood flow, air flow, volume change, and lung pressure-volume curve) could be used to alter the motions. We are already working on developing a finite-element representation of the heart.[37]

In terms of modeling anatomical variations with the XCAT, each new anatomy is ultimately derived from the template adult anatomies based on the Visible Human data. We are currently working to expand the XCAT library of anatomies beyond the Visible Human adults by developing a series of template phantoms with ages ranging from newborn to adult[38,39] based on several MSCT datasets of normal subjects. Each phantom will be defined based on segmentation of the MSCT data and using the template XCAT anatomies (transformed to fit the segmented framework) to fill in missing or hard to segment structures. These new XCAT phantoms can serve as springboards from which to create patient populations at different ages.
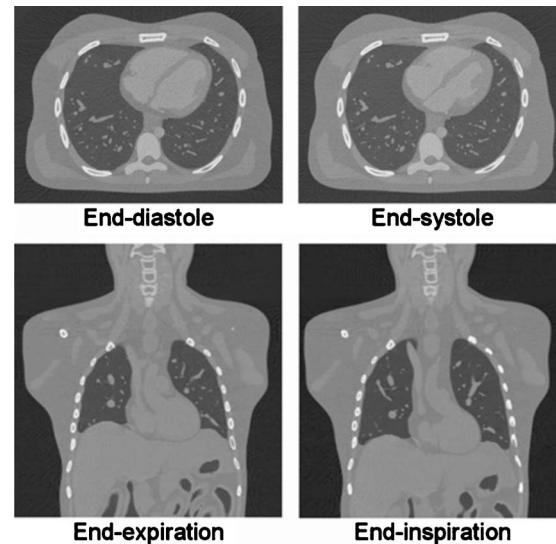
Another limitation to the XCAT is that breast models are simple surfaces and do not include any interior anatomical detail. We are currently developing a series of detailed 3D computational breast models to incorporate into the female XCAT for breast imaging research[40] based on high-resolution dedicated breast CT data. When complete, the models will be capable of realistically simulating a wide range of anatomical variations in health and disease and will include finite-element-based techniques to simulate different compression states of the breast for various imaging modalities.

With the increased use of computer-based imaging simulation, we conclude that the new 4D XCAT phantom, with its ability to produce realistic predictive imaging data from anatomically diverse patients of known anatomy, will provide an important tool in multimodality imaging research to evaluate and compare imaging devices and techniques. It will provide an efficient means with which to determine the best methods or combination of methods for patient diagnosis and treatment.

Specifically for CT imaging, the phantom may provide the necessary foundation to optimize clinical CT applications so as to obtain the highest possible image quality with the minimum possible radiation dose to the patient, an area of research that is becoming more significant with the proliferation of CT protocols. Using existing CT simulators, the phantom can be imaged repeatedly under many different scanning conditions and parameters without any fear of radiation exposure. Effects of acquisition parameters, physical processes, and patient anatomy and motion can all be studied within simulated images. Combined with accurate Monte Carlo methods to estimate dose such as the one developed in our laboratory,[41] the radiation exposure to the phantom for each procedure may be simultaneously calculated to assess the trade-off between image quality and radiation dose. Due

to radiation concerns in patients and the limited number of physical phantoms, such research can only be performed using realistic computational phantoms.

ACKNOWLEDGMENT

a)Author to whom correspondence should be addressed. Electronic mail: paul.segars@duke.ed; Telephone: 919-684-1473.

[1] M. Caon, "Voxel-based computational models of real human anatomy: A review," Radiat. Environ. Biophys. **42**, 229–235 (2004).

[2] M. Cristy and K. F. Eckerman, "Specific absorbed fractions of energy at various ages from internal photon sources," ORNL Report No. TM-8381 (Oak Ridge National Laboratory, TN, 1987).

[3] W. P. Segars, "Development of a new dynamic NURBS-based cardiac-torso (NCAT) phantom," Ph.D. dissertation, The University of North Carolina, 2001.

[4] C. Lee, D. Lodwick, J. Hurtado, D. Pafundi, J. Lwilliams, and W. E. Bolch, "The UF family of reference hybrid phantoms for computational radiation dosimetry," Phys. Med. Biol. **55**, 339–363 (2010).

[5] L. Piegl, "On NURBS: A survey," IEEE Comput. Graphics Appl. **11**, 55–71 (1991).

[6] L. Piegl and W. Tiller, *The NURBS Book* (Springer-Verlag, New York, 1997).

[7] W. P. Segars, D. S. Lalush, and B. M. W. Tsui, "A realistic spline-based dynamic heart phantom," IEEE Trans. Nucl. Sci. **46**, 503–506 (1999).

[8] W. P. Segars, D. S. Lalush, and B. M. W. Tsui, "Modeling respiratory mechanics in the MCAT and spline-based MCAT phantoms," IEEE Trans. Nucl. Sci. **48**, 89–97 (2001).

[9] Visible Human Male and Female datasets, http://www.nlm.nih.gov/research/visible/visible_human.html, National Library of Medicine.

[10] X. He, E. C. Frey, J. M. Links, K. L. Gilland, W. P. Segars, and B. M. Tsui, "Effect of anatomical and physiological factors and compensation methods on observer of performance for defect detection in myocardial perfusion," J. Nucl. Med. **44**, 112P–112P (2003).

[11] B. M. W. Tsui and W. P. Segars, "Applications of computer generated phantoms to medical imaging and dosimetry calculations," *Handbook of Anatomical Models for Radiation Dosimetry* (Informa Healthcare, New York, NY, 2009), pp. 549–566.

[12] R. McNeil, RHINOCEROS, 1.0 ed., Seattle, WA, 1998.

[13] H. Hoppe *et al.*, "Piecewise smooth surface reconstruction," Comput. Graph. **28**, 295–302 (1994).

[14] C. Loop, "Smooth subdivision surfaces based on triangles," Thesis, University of Utah, 1987.

[15] J. M. Garrity, W. P. Segars, S. B. Knisley, and B. M. W. Tsui, "Development of a dynamic model for the lung lobes and airway tree in the NCAT phantom," IEEE Trans. Nucl. Sci. **50**, 378–383 (2003).

[16] J. Park, D. N. Metaxas, A. A. Young, and L. Axel, "Deformable models with parameter functions for cardiac motion analysis from tagged MRI data," IEEE Trans. Med. Imaging **15**, 278–289 (1996).

[17] W. P. Segars, T. S. Lee, and B. M. W. Tsui, "Simulation of motion defects in the 4D NCAT cardiac model," J. Nucl. Med. **44**, 142P–142P (2003).

[18] W. P. Segars, G. T. Y. Chen, and B. M. W. Tsui, "Modeling respiratory motion variations in the 4D NCAT phantom," IEEE Nuclear Science Symposium/Medical Imaging Conference, Honolulu, HI, 2007, pp. 2677–2679 (unpublished).

[19] ICRP, "Basic anatomical and physiological data for use in radiological protection: reference values," ICRP Publication 89 (International Commission on Radiological Protection, New York, NY, 2002).

[20] J. Foley, A. van Dam, S. Feiner, and J. Hughs, *Computer Graphics*, 2nd ed. (Addison-Wesley, New York, 1997).

[21] A. Watt and M. Watt, *Advanced Animation and Rendering Techniques* (Addison-Wesley, New York, 1998).

[22] S. Jan *et al.*, "GATE: A simulation toolkit for PET and SPECT," Phys. Med. Biol. **49**, 4543–4561 (2004).

[23] M. Ljungberg and S.-E. Strand, "A Monte Carlo program for the simulation of scintillation camera characteristics," Comput. Methods Programs Biomed. **29**, 257–272 (1989).

[24] Y. Du, E. C. Frey, W. T. Wang, C. Tocharoenchai, W. H. Baird, and B. M. W. Tsui, "Combination of MCNP and SimSET for Monte Carlo simulation of SPECT with medium- and high-energy photons," IEEE Trans. Nucl. Sci. **49**, 668–674 (2002).

[25] T. H. Jochimsen and M. von Mengershausen, "ODIN—Object-oriented development interface for NMR," J. Magn. Reson. **170**, 67–78 (2004).

[26] H. Benoit-Cattin, G. Collewet, B. Belaroussi, H. Saint-Jalmes, and C. Odet, "The SIMRI project: A versatile and interactive MRI simulator," J. Magn. Reson Imaging **173**, 97–115 (2005).

[27] J. Sempau, J. M. Fernandez-Varea, E. Acosta, and F. Salvat, "Experimental benchmarks of the Monte Carlo code PENELOPE," Nucl. Instrum. Methods Phys. Res. B **207**, 107–123 (2003).

[28] W. P. Segars, M. Mahesh, T. J. Beck, E. C. Frey, and B. M. W. Tsui, "Realistic CT simulation using the 4D XCAT phantom," Med. Phys. **35**, 3800–3808 (2008).

[29] J. A. Jensen, "Ultrasound imaging and its modeling," *Imaging of Complex Media with Acoustic and Seismic Waves* (Springer, Berlin/Heidelberg, 2002), pp. 135–165.

[30] T. D. Mast, L. M. Hinkelman, L. A. Metlay, M. J. Orr, and R. C. Waag, "Simulation of ultrasonic pulse propagation, distortion, and attenuation in the human chest wall," J. Acoust. Soc. Am. **106**, 3665–3677 (1999).

[31] R. Harrison, D. Haynor, S. Gillespie, S. Vannoy, M. Kaplan, and T. Lewellen, "A public-domain simulation system for emission tomography: photon tracking through heterogeneous attenuation using importance sampling," J. Nucl. Med. **34**(5), 60 (1993).

[32] K. Wienhard *et al.*, "The ECAT HRRT: Performance and first clinical application of the new high resolution research tomograph," IEEE Trans. Nucl. Sci. **49**, 104–110 (2002).

[33] P. P. Bruyant, "Analytic and iterative reconstruction algorithms in SPECT," J. Nucl. Med. **43**, 1343–1358 (2002).

[34] B. M. W. Tsui, H.-B. Hu, and D. R. Gilland, "Implementation of simultaneous attenuation and detector response correction in SPECT," IEEE Trans. Nucl. Sci. **35**, 778–783 (1988).

[35] G. L. Zeng and G. T. Gullberg, "Frequency domain implementation of the three-dimensional geometric point response function correction in SPECT imaging," IEEE Nuclear Science Symposium and Medical Imaging Conference, Santa Fe, NM, 1991, pp. 1943–1947 (unpublished).

[36] K. Cranley, B. Gilmore, G. Fogarty, and L. Desponds, Catalogue of Diagnostic X-Ray Spectra and Other Data, Diagnostic Radiology and Magnetic Resonance Special Interest Group of the Institute of Physics and Engineering in Medicine.

[37] A. I. Veress, W. P. Segars, B. M. W. Tsui, J. A. Weiss, and G. T. Gullberg, "Normal and pathological NCAT image and phantom data based on physiologically realistic left ventricle finite element models," IEEE Trans. Med. Imaging **25**(12), 1604–1616 (2006).

[38] X. Li, E. Samei, W. P. Segars, G. Sturgeon, J. G. Colsher, and D. Frush, "Patient-specific dose estimation for pediatric CT," Med. Phys. **35**, 5821–5828 (2008).

[39] W. P. Segars *et al.*, "Transformable computational phantom for optimization of x-ray CT imaging protocols," IEEE Nuclear Science Symposium/Medical Imaging Conference, Honolulu, HI, 2007, pp. 2677–2679 (unpublished).

[40] C. M. Li, W. P. Segars, J. Y. Lo, A. Veress, J. M. Boone, and J. T. Dobbins, "Methodology for generating a 3D computerized breast phantom from empirical data," Med. Phys. **36**, 3122–3131 (2009).

[41] X. Li, E. Samei, T. T. Yoshizumi, J. G. Colsher, R. Jones, and D. Frush, "Experimental benchmarking of a Monte Carlo dose simulation code for pediatric CT," SPIE Medical Imaging Conference, San Diego, CA, 2008 (unpublished).